New evidence for dislocation creep from 3-D geodynamic modeling the Pacific upper mantle structure

Jeroen van Hunen[1,2*], Shijie Zhong[1], Nikolai M. Shapiro[1], and Michael H. Ritzwoller [1]

[1]Department of Physics, University of Colorado at Boulder
Campus Box 390, Boulder, CO 80309-0390 USA
[2]Institute of Geophysics, ETH Zurich, Switzerland

[*]To whom correspondence should be addressed; E-mail: hunen@erdw.ethz.ch

Laboratory studies on deformation of olivine in response to applied stress suggest two distinct deformation mechanisms in the Earth's upper mantle: diffusion creep through diffusion of atoms along grain boundaries and dislocation creep by slipping along crystallographic glide planes (*1, 2*). Each mechanism has very different and important consequences on the dynamical evolution of the mantle and the development of mantle fabric. However, due to the lack of in-situ observations, it is unclear which deformation mechanism dominates in the upper mantle. By studying the thermo-mechanical erosion of the lithosphere by thermal boundary layer instabilities in 3D dynamical models, this study demonstrates that the thermal structure of the Pacific lithosphere and upper mantle, as revealed by recent seismic models (*3*), requires that the predominant deformation mechanism in the upper mantle is dislocation creep

with an activation energy of about 360 kJ/mol, consistent with that for dislocation creep for olivine determined from laboratory studies.

In the last thirty years, significant progress has been made in determining deformational properties (i.e., rheology) of olivine under laboratory conditions. In particular, with increasing accuracy, experimental studies have determined rheological activation parameters (e.g., activation energy) for wet and dry olivine undergoing diffusion creep and dislocation creep – the two most important deformation mechanisms in the mantle (*1, 2, 4*). It is important to test the experimental results against in-situ mantle processes, because the experiments are done under conditions (e.g., strain rate) that are dramatically different from those in the mantle. It is critically important to test which deformation mechanism is predominant in the mantle, given the significance of implications of the mechanism of deformation for the structure and dynamics of the mantle (*5*). Post-glacial rebound (PGR)studies reveal that the average mantle viscosity for the top 1200 km of the mantle is about 10^{21} Pa s (*6*). However, because of limited resolution, PGR studies cannot distinguish dislocation from diffusion creep mechanisms (*1, 7*). Other observational constraints on mantle viscosity such as long- wavelength geoid anomalies (*8*) suffer similar limitations. Observations of seismic anisotropy in the upper mantle (*9, 10*), if caused by lattice preferred orientation (LPO), would be consistent with the upper mantle being dominated by dislocation creep (*1*). However, mantle melts and shape preferred orientation of mantle minerals may also induce anisotropy (*1*).

By contrasting geodynamical models of sub-lithospheric boundary layer instabilities with recent results from seismic tomography of the Pacific upper mantle, this study provides new evidence that the upper mantle is dominated by dislocation creep with an activation energy that is consistent with laboratory values. The thermal structure of the Pacific lithosphere and upper mantle is deduced from a seismological model (*3*) (Figure 1). A striking feature of the seismic model is that the Pacific lithosphere older than about 70 Ma is significantly hotter than that

predicted from a conductive cooling model (*11*) and that the deviation is mainly a function of lithospheric age t_l. Lithospheric thermal structure is quantified as an "apparent thermal age" t_a (*3*), which is defined as the lithospheric age at which a purely conductive temperature profile would most closely resemble the observed thermal structure. Comparing t_a with lithospheric age t_l reveals that t_a is insensitive to t_l between 70 and 100 Ma, although it increases steadily with age for both younger and older lithosphere (Figure 1c).

This thermal structure of the Pacific uppermost mantle suggests a period of lithospheric reheating between 70 and 100 Ma. Physical processes to explain such reheating include both shallow and deep origins. Thermal boundary layer instabilities (TBI) could erode the deeper parts of the lithosphere, as suggested previously on the basis of seafloor topography, gravity and heat flow (*12–16*). Although TBI could be triggered by the impingement of mantle plumes (*17*), the clear age-dependence of the seismic results prompts us to focus on shallower processes – namely, spontaneous TBI (*12, 18*).

Significant progress in the understanding of TBI with realistic mantle rheology has been achieved in the last decade through both laboratory and numerical studies (*18–23*), which can be summarized as follows. As the lithosphere cools and thickens with time, the bottom part of the lithosphere becomes gravitationally unstable and is eroded by the TBI. The degree of such erosion is determined by the activation energy E^*. Decreasing E^* increases the portion of the lithosphere that is eroded, and enhances lithospheric reheating. This is because the smaller E^* leads to a smaller increase in lithospheric viscosity with decreasing temperature, and that only the portion of lithosphere with viscosity that is less than a factor of 10 larger than the underlying mantle can participate in the TBI and be eroded (*18*).

However, previous studies were performed with 2-D models with diffusion creep deformation (i.e., Newtonian rheology) and no plate motion. To quantify the effects of thermo-mechanical erosion and compare with seismic observations, we formulate a 3-D Cartesian

model of mantle convection that includes both dislocation and diffusion creep deformation mechanisms and plate motion (Figure 2). The flow and temperature of the oceanic upper mantle down to 670 km with 8.6 cm/year surface plate motion and flow-through boundary conditions are solved with a finite element formalism (*24, 25*). This model simulates the cooling of the lithosphere and the resulting TBI for various rheological conditions (*26*). For either deformation mechanism, we may use a power-law Arrhenius rheology $\dot{\epsilon} = A\sigma^n \exp(-E^*/RT)$, where $\dot{\epsilon}, \sigma, R, T, A$, and n are the strain rate, stress, gas constant, temperature, rheology prefactor and exponent, respectively. The exponent n is equal to 1 and 3.5 for diffusion and dislocation creep, respectively. The model is divided into two layers: a 400 km thick upper mantle layer where either diffusion or dislocation creep is used, and a bottom layer (i.e., transition zone) with diffusion creep. We choose the upper mantle viscosity so that the onset of TBI is approximately at 70 Ma (*21*), and a transition zone viscosity higher by about a factor of 50 (*8*). Our models are time-dependent, and we present model results after a statistical steady-state is reached.

We first present a model in which dislocation creep is the dominant mechanism with $n = 3.5$ in the upper mantle to elucidate the effects of the TBI on the thermal and rheological state of the upper mantle and lithosphere (Fig. 2). For this model, E^*=360 KJ/mol, and the TBI starts when the lithosphere reaches an age of about 70 Ma or at a distance of about 6000 km from the mid-ocean ridge (MOR). The average effective viscosity in the asthenosphere is 1.5×10^{19} Pa s. The convective structure has a tendency to align with the plate motion, but significant variations exist in directions both perpendicular and parallel to plate motion, particularly at large depths (Figures 2a-2c). At the onset of the TBI, the typical wavelength of plate motion-parallel structure is around 200 km. The wavelength becomes more variable and irregular at larger distances from the MOR, implying significant re-organization of the structure. This structure is significantly different from the roll structure reported in early laboratory studies of plate-driven instabilities for fluids with relatively uniform properties (*27*).

The TBI leads to erosion of lithospheric material and an increase in lithospheric temperature (Figures 2a-2c). Consequently, after the onset of TBI, the lithosphere thickens less rapidly or sometimes thins with age. For this model, the 1250^oC-isotherm is lifted up on average by about 15 to 20 km. At the onset of TBI, the increased deformation rate due to the non-linear mantle rheology reduces the effective viscosity (Figure 2d), which in turn further enhances the instability. After this first phase of instability, lithosphere thickens again, but a difference in thickness with 'undisturbed' lithosphere remains.

To compare this model with the seismic results we estimate the apparent thermal age t_a at a given lithospheric age t_l or x. An averaged temperature is calculated over all lithosphere of given t_l or x over the top 150 km. t_a is the age that gives the same average temperature from a purely conductive model of lithosphere (*11*). The estimated t_a (Figure 3) clearly reflects the lithospheric thickness variations: it closely follows lithospheric age t_l until TBI occurs, but is reduced considerably during the first phase of TBI before it starts to increase again after about 10 Ma. t_a remains smaller than t_l by about 25 Ma after age of 75 Ma. This increasing deviation of t_a from t_l around 70 Ma and the subsequent nearly constant deviation for older lithosphere closely resemble average seismic thermal structures (Figure 3), and strongly suggest that the TBI is the mechanism that is responsible for the seismic observations.

We performed similar calculations for different values of the activation energy E^* for both diffusion creep ($n = 1$), and dislocation creep ($n = 3.5$) for the upper mantle. All cases display similar dynamics for the TBI, particularly for the relation between t_a and t_l (Figure 3). The main difference between cases with different E^* is that reducing E^* increases the thermo-mechanical erosion of the lithosphere and increases the deviation between t_a and t_l. This is consistent with the suggestion that E^* controls temperature anomalies associated with the TBI (*18*). The main difference between diffusion and dislocation creep cases is that the first phase of TBI is not as strong for $n = 1$ as for $n = 3.5$, as indicated by more gentle variations of t_a with t_l (Figure 3).

For diffusion creep deformation, E^* needs to be as small as 120 kJ/mol to produce sufficient lithospheric erosion to fit the seismic results (Figure 3). Larger E^* results in too small lithospheric erosion or deviations of t_a from t_l. The two cases with E^* of 360 and 540 kJ/mol for dislocation creep reproduce the seismic results reasonably well. Estimates of E^* for diffusion creep from experimental studies for olivine aggregates are 375 kJ/mol with 20% uncertainty (*2, 28*), while E^* for dislocation creep is estimated to be 470 and 510 kJ/mol (with 10% uncertainty) for wet and dry conditions, respectively (*4, 29*). While the experimental estimates of E^* for diffusion creep are much higher than our best fit value of 120 kJ/mol for diffusion creep, for dislocation creep the acceptable range of E^* up to 540 kJ/mol is consistent with laboratory values. This suggests that deformation in the upper mantle below the Pacific is accomplished predominantly by dislocation creep and not by diffusion creep.

In addition to explaining the Pacific upper mantle and lithospheric seismic structure, these models of the TBI have other important implications. 1) The dominant deformation mechanism in the upper mantle being dislocation creep suggests an LPO-origin for seismic anisotropy and provides further evidence for a relationship between seismic anisotropy and mantle flow and deformation (*30*). 2) Our results confirm laboratory measurements of rheological activation energy and their applicability to mantle processes. 3) By reheating the oceanic lithosphere, the TBI process may significantly affect the thermo-mechanical structure of the lithosphere. This may influence seafloor topography and heat flux (*12*) and the dynamics of subduction (*20*). 4) The TBI provides an explanation for seismically observed small-scale structures (i.e., smaller than the plate-scale) in the upper mantle (*31*). Higher resolution seismic studies that map small-scale upper mantle structures will help further constrain the mantle dynamics and rheology.

References and Notes

1. S.-i. Karato, P. Wu, *Science* **260**, 771 (1993).

2. G. Hirth, D. L. Kohlstedt, *The subduction factory*, J. Eiler, ed. (American Geophysical Union, Washington D. C., 2003).

3. M. H. Ritzwoller, N. M. Shapiro, S. Zhong, *Earth Plan. Sci. Let.* **226**, 69 (2004).

4. S.-i. Karato, H. Jung, *Philosophical Magazine* **83(3)**, 401 (2003).

5. U. R. Christensen, *Geoph.J.R.Astron.Soc.* **77**, 242 (1984).

6. J. X. Mitrovica, *J. Geophys. Res.* **101**, 555 (1996).

7. P. Wu, *Geophys. J. Int.* **108**, 35 (1992).

8. B. H. Hager, M. A. Richards, *Phil. Trans. R. Soc. Lond.* **328**, 309 (1989).

9. J.-P. Montagner, T. T., *J. Geophys. Res.* **96**, 20337 (1991).

10. G. Ekström, A. M. Dziewonski, *Nature* **394**, 168 (1998).

11. D. L. Turcotte, G. Schubert, *Geodynamics, Applications of continuum physics to geological problems, Second Edition* (Cambridge University Press, 2002).

12. B. Parsons, D. McKenzie, *J. Geophys. Res.* **83**, 4485 (1978).

13. C. A. Stein, S. Stein, *Nature* **359**, 123 (1992).

14. S. Nagihara, C. R. B. Lister, J. G. Sclater, *Earth Plan. Sci. Let.* **139**, 91 (1996).

15. W. F. Haxby, J. K. Weissel, *J. Geophys. Res.* **91**, 3507 (1986).

16. W. R. Buck, E. M. Parmentier, *J. Geophys. Res.* **91**, 1961 (1986).

17. W. B. Moore, G. Schubert, P. Tackley, *Science* **279**, 1008 (1998).

18. A. Davaille, C. Jaupart, *J. Geophys. Res.* **99**, 19853 (1994).

19. C. Dumoulin, M.-P. Doin, L. Fleitout, *Phys. Earth Planet. Inter.* **125**, 45 (2001).

20. C. P. Conrad, B. H. Hager, *J. Geophys. Res.* **104**, 17551 (1999).

21. J. Huang, S. Zhong, J. van Hunen, *J. Geophys. Res.* **108(B8)**, 2405, 10.1029/2003JB002456 (2003).

22. J. Korenaga, T. H. Jordan, *J. Geophys. Res.* **108**, 2333,10.1029/2002JB001760 (2003).

23. S. Zaranek, E. Parmentier, *J. Geophys. Res.* **109**, B03409, doi:10.1029/2003JB002462 (2004).

24. L. Moresi, M. Gurnis, *Earth Plan. Sci. Let.* **138**, 15 (1996).

25. S. Zhong, M. T. Zuber, L. Moresi, M. Gurnis, *J. Geophys. Res.* **105**, 11063 (2000).

26. J. van Hunen, J. Huang, S. Zhong, *Geophys. Res. Let.* **30(19)**, 1991, 10.1029/2003GL018101 (2003).

27. F. M. Richter, B. Parsons, *J. Geophys. Res.* **80**, 2529 (1975).

28. S. Mei, D. L. Kohlstedt, *J. Geophys. Res.* **105**, 21457 (2000).

29. S. Mei, D. L. Kohlstedt, *J. Geophys. Res.* **105**, 21471 (2000).

30. P. Silver, W. Holt, *Science* **295**, 1054 (2002).

31. R. Katzman, L. Zhao, T. H. Jordan, *J. Geophys. Res.* **103**, 17933 (1998).

32. M. H. Ritzwoller, N. M. Shapiro, M. P. Barmin, A. L. Levshin, *J. Geophys. Res.* **107**, 2335, doi:10.1029/2002JB001777 (2002).

33. G. Ekström, J. Tromp, E. Larson, *J. Geophys. Res.* **102**, 8137 (1997).

34. J. Trampert, J. Woodhouse, *gji* **122**, 675 (1995).

35. N. M. Shapiro, M. H. Ritzwoller, *Geophys. J. Int.* **51**, 88 (2002).

36. N. M. Shapiro, M. H. Ritzwoller, *Geophys. J. Int.* **157**, 1175 (2004).

37. This study is funded by the David and Lucile Packard Foundation and the US NSF grants EAR 0134939 and EAR 0409217.

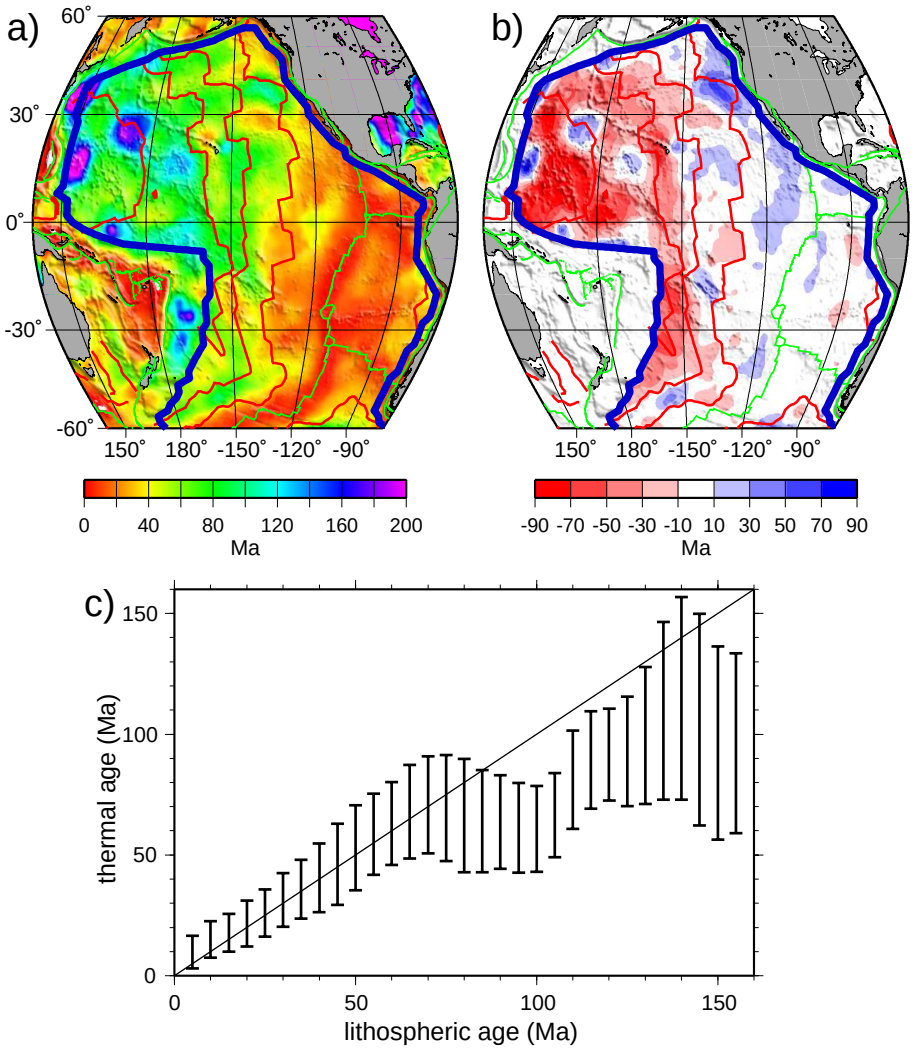

Figure 1: Seismic results from (*3*). Inversion for a radially anisotropic 3-D tomographic model of shear-wave velocity and temperature of the Pacific upper mantle is performed in two steps: 1) Construction of Rayleigh and Love wave group velocity maps (*32*) on a 2×2^o grid across the Pacific, and a phase velocity map using measurements compiled at Harvard (*33*) and Utrecht (*34*) Universities. 2) Dispersion map inversion (*35*) produces a thermal 3-D model on a 2×2^o grid to 400 km depth based on a thermal parameterization (*36*). a) Apparent thermal age t_a from the seismic inversion. b) Difference between lithospheric age t_l and t_a. c) t_a-distribution for given t_l, collected in 5-Ma age bins. Vertical bars represent standard deviations in age bins from the seismic results.

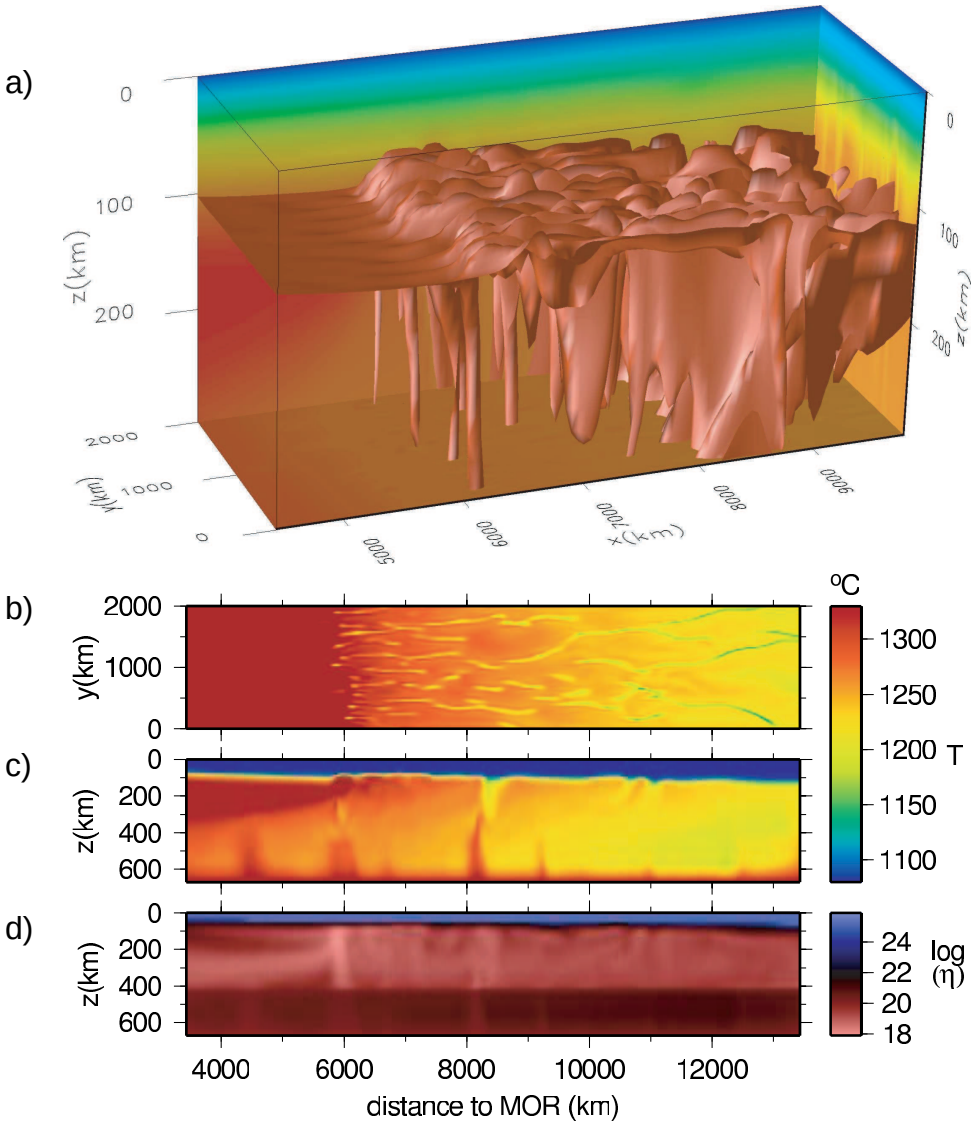

Figure 2: 3-D numerical models are performed in a 670 km-deep box of 14000 km length in the x-direction and 2000 km in the y-direction. Flow-through boundary conditions (*26*) are employed with leftward surface plate motion of 8.6 cm/yr relative to the non-moving bottom boundary and temperature structure corresponding to that for 5 Ma-old oceanic lithosphere at inflow. The temperatures at the surface and bottom boundaries are fixed at $T = 0^o$C and $T = 1350^o$C, respectively. The effective Rayleigh number $Ra_{\text{eff}} = 3 \times 10^7$ is defined using the asthenospheric viscosity, and is chosen such that TBI starts around 70 Ma. A representative snapshot of thermal and rheological structures is shown for a model with $E^* = 360$ kJ/mol, and $n = 3.5$. a) 3-D view of the temperature field (1250^oC-isotherm) for the top 300 km of the model domain with a 10-fold vertical exaggeration. b) Horizontal temperature cross section at 150 km depth. c) Vertical temperature cross-section at $y = 1000$ km. d) Vertical cross section of the effective viscosity η at $y = 1000$ km. $\eta \approx 1.5 \cdot 10^{19}$ Pa s in the asthenosphere, and about 50 times larger in the transition zone.

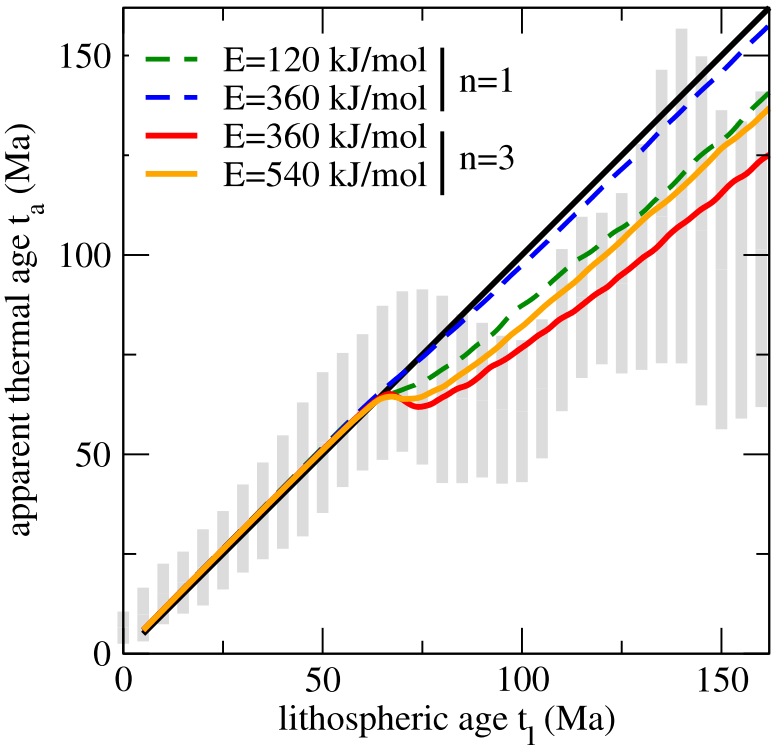

Figure 3: Apparent thermal age versus lithospheric age from the seismic results (grey bars, also see Figure 1) and numerical model results (lines).